ARTICLES
https://doi.org/10.1038/s41565-018-0330-9
nature nanotechnology

Microfluidics-enabled orientation and microstructure control of macroscopic graphene fibres

Guoqing Xin, Weiguang Zhu, Yanxiang Deng, Jie Cheng, Lucy T. Zhang, Aram J. Chung, Suvranu De and Jie Lian*

Macroscopic graphene structures such as graphene papers and fibres can be manufactured from individual two-dimensional graphene oxide sheets by a fluidics-enabled assembling process. However, achieving high thermal-mechanical and electrical properties is still challenging due to non-optimized microstructures and morphology. Here, we report graphene structures with tunable graphene sheet alignment and orientation, obtained via microfluidic design, enabling strong size and geometry confinements and control over flow patterns. Thin flat channels can be used to fabricate macroscopic graphene structures with perfectly stacked sheets that exhibit superior thermal and electrical conductivities and improved mechanical strength. We attribute the observed shape and size confinements to the flat distribution of shear stress from the anisotropic microchannel walls and the enhanced shear thinning degree of large graphene oxide sheets in solution. Elongational and step expansion flows are created to produce large-scale graphene tubes and rods with horizontally and perpendicularly aligned graphene sheets by tuning the elongational and extensional shear rates, respectively.

Macroscopic graphene fibres can be manufactured by fluidics-enabled assembly from two-dimensional (2D) graphene oxide (GO) sheets dispersed in aqueous solutions to form lyotropic liquid crystal[1,2]. Due to the anisotropic liquid-crystal behaviour of the GO precursors, pre-aligned GO sheets can be directed under the shear flow to form an ordered assembly in a macroscopic fibre structure via a simple and cost-effective wet-spinning process[3–10]. Graphene fibres can be produced upon chemical or thermal reduction of the precursor GO fibres with partially/completely removed oxygen functional groups and defects[6,10].

The fine control of microstructure and graphene sheet alignment is critical to the thermal-mechanical properties of the assembled graphene fibres. Highly aligned sp^2 graphene sheets and macroscopic order of the graphitic domains are necessary to achieve high thermal and electrical properties and high Young's modulus[11,12]. However, the mechanical strength of the graphene fibres is primarily limited by the van der Waals interaction between the graphene sheets[6–10,13]. Heterogeneous structures including functional groups and sp^3 bonds or a turbostratic arrangement of graphitic domains improve the mechanical strength, as in polyacrylonitrile (PAN)-based carbon fibres[11,12], but these heterogeneous structures behave as effective phonon and electron scattering centres, reducing the electrical and thermal conductivities. Therefore, it is very challenging to simultaneously realize high thermal/electrical and mechanical properties in graphene fibres.

Recently, a highly thermally conductive and mechanically strong graphene fibre was demonstrated by intercalating small-sized GO sheets into large-sized GO sheets to improve fibre compactness and physical density[6]. High-temperature carbonization and graphitization were applied to improve the crystallinity, graphene sheet alignment and macroscopic ordering to achieve high thermal conductivity and mechanical strength (>1 GPa)[6]. However, unlike conventional carbon fibres[14–16], fine control of the sheet alignment and orientation of the fibre structure remains limited and the microstructure is not optimized due to the intrinsic issues arising from the shear-stress-induced self-assembly process[6,9]. Control of the thermal-mechanical properties and how different wet-spinning processes affect the fluidics-assisted assembly are yet to be elucidated.

Intuitively, the wet-spinning process used to obtain graphene fibres from individual GO sheets restricts the fine control of fibre structure to a lower degree of sheet alignment, high porosity, rough surface morphology and a non-uniform core–sheath structure, thus limiting their mechanical and physical properties[6,9]. In particular, a skin effect occurs during the fluidic flow-assisted assembly process, leading to a core–shell structure (Supplementary Fig. 1)[6,9] and degrading the mechanical and transport properties. The core–shell structure, with well-aligned graphene sheets on fibre surfaces but random sheet alignments and a turbostatic arrangement of graphitic domains along the transverse direction and inner graphene fibre geometry, is mainly induced by the flow shear stress gradient along the transverse direction of the microchannel. Further confinement of the fibres into smaller diameters can mitigate the core–shell structure and thus improve mechanical strength (up to 1.45 GPa)[9]. However, the achieved mechanical strength and Young's modulus are still inferior to these of PAN-based or meso-phase pitch-based carbon fibres[6,9,12].

Additionally, the rheological properties of the GO sheets during fluidic flow are controlled by the GO sheet concentration, flow rate and their interaction within the confined geometry of the microfluidic channels, significantly impacting the graphene sheet alignment of the precursor GO and final graphene fibres. For fluid flows through microchannels, standard macromolecules typically have lengths below 10 nm and large colloidal particles of 100 nm, and are therefore negligible in size even in micrometre-sized confining volumes[17]. However, with a substantial increase of lateral size of the GO sheets, approaching the size of the microchannels, the fluidic-assisted

Department of Mechanical, Aerospace and Nuclear Engineering, Rensselaer Polytechnic Institute, Troy, NY, USA. *e-mail: lianj@rpi.edu

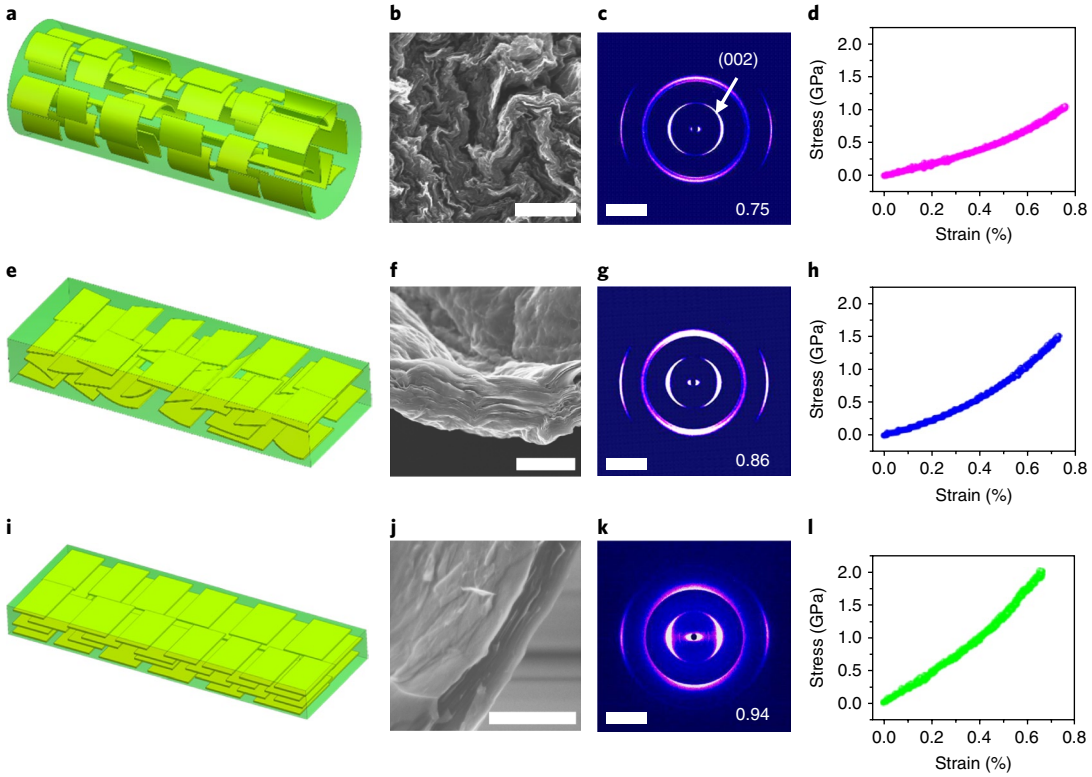

Fig. 1 | Size and shape confinements controlling sheet orientation in solution and thus the microstructure and mechanical properties of the annealed graphene structures. The higher order of the GO sheets in fluid flow can be directly transferred to a higher order of alignment and orientation of graphene sheets in the final graphene fibres, leading to an almost 100% improvement in the fracture strength of the fibre. **a**, Curved and distorted 2D GO sheets flowing in a tubular channel. **b**, Wrinkled sheets in the cross-section of the columnar fibre produced from a tubular channel. **c**, Long arc and dispersed intensity of the characteristic (002) reflection on WAXS patterns, indicating low sheet orientation along the fibre axis direction. **d**, Inferior mechanical properties of the columnar fibre. **e**, Arranged GO sheets flowing in an anisotropic flat channel. **f**, A layer structure of a graphene belt assembled by a flat channel. **g**, Narrow dispersion of the (002) plane on WAXS patterns, indicating enhanced sheet orientation order. **h**, Improved mechanical properties of the graphene belt. **i**, GO sheets are neatly organized when flowing in a thinner flat channel. **j**, A highly ordered and compact structure of a thin graphene belt. **k**, A high degree of sheet orientation indicated by the concentrated short arc of the (002) plane on the WAXS pattern. **i**, Exceptional mechanical strength of the thin graphene belt. Bottom inset numbers in **c**, **g** and **k** are order parameters calculated from the (002) planes on WAXS patterns. Scale bars, 1 μm (**b**), 1 μm (**f**), 0.5 μm (**j**), and 20 nm^{-1} (**c**,**g**,**k**).

assembly is significantly impacted by the dimensions of the GO sheets and microchannels, offering an opportunity to tune the graphene sheet alignment and microstructure. The highly anisotropic geometry of the 2D GO sheets, with a large aspect ratio (>10,000)[18], may provide another degree of freedom for controlling GO flow patterns and thus sheet orientation by tuning the geometrical shape of the microchannel.

Current mainstream manufacturing processes, such as wet spinning[6], self-assembly[19] and vacuum filtration[20], only allow the alignment of graphene/GO sheets flatwise into a layered structure. Macroscopic graphene structures with vertically aligned sheets have not yet been realized with a direct assembly process. Nor has there been a demonstration of the fabrication of macroscopic graphene structures or microstructure control from perfectly horizontally stacked to vertically aligned graphene sheet and domain arrangements. A 3D open architecture of vertically aligned graphene structures may be useful for enhancing the energy storage performance of supercapacitors/batteries by improving ion transport and accessibility[21]. Furthermore, vertically aligned graphene sheet structures may bring substantial benefits to heat transfer efficiency along both lateral and vertical directions for graphene-based thermal management systems[22].

Here, we demonstrate the concepts of using shape and size confinement for the fine control of sheet alignment and orientation during fluidic-flow enabled assembly of macroscopic graphene structures (Fig. 1) as well as the flexibility of tailoring their microstructures by controlling flow patterns (Fig. 2), allowing manipulation of the sheet orientation direction and improvements in properties. The effects of the rheological properties of the GO dispersion and the flow patterns on the fluidics-enabled assembly of macroscopic structures are explored. The scientific correlation among the microfluidics-enabled assembly/microstructure control/properties is established, enabling new sciences to optimize fibre assembly and microstructure to develop high-performance graphene fibres.

Concepts of microfluidics-enabled orientation control

When 2D GO sheets are flowing in a tubular channel they become curved and distorted as a result of the mismatching of the geometries of the sheets and the channel (Fig. 1a). A random orientation of sheets with heavy wrinkles and defective voids is observed on the cross-section of a columnar fibre spun from a tubular channel (Fig. 1b), leading to lower order parameter (of 0.75) and sheet orientation degree, as measured by wide-angle X-ray scattering (WAXS)[23] (Fig. 1c and Supplementary Fig. 2). The less ordered structure results in low mechanical strength and modulus (Fig. 1d). In contrast, GO sheets are well arranged when flowing in a flat channel with a compatible geometry (Fig. 1e).

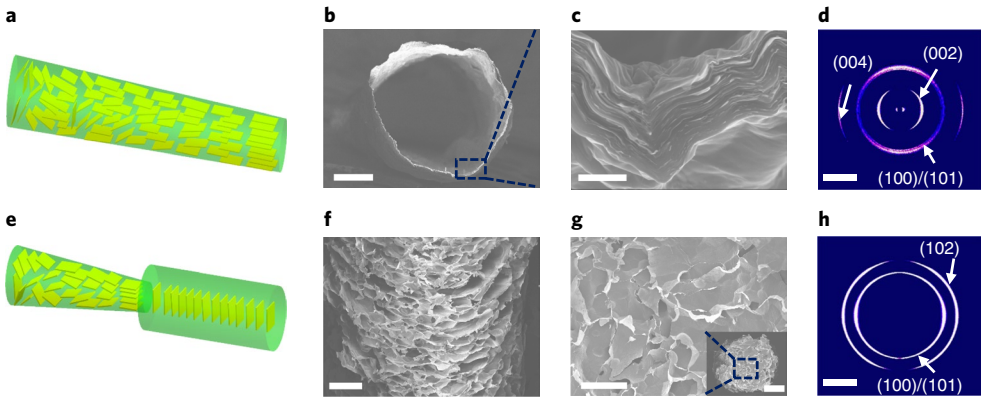

Fig. 2 | Contraction and step expansion flow patterns for horizontally and vertically aligned graphene structures. a, Dramatically improved sheet orientation of GO solution flowing in a contracted channel. **b**,**c**, Graphene tubes (**b**) produced from a contraction flow with compact and well-stacked sheets inside tube walls (**c**). **d**, Narrow dispersed arc of the (002) plane representing high sheet orientation order inside the tube wall. **e**, Inversing the sheet orientation direction by pumping GO solution from a contracted channel into a suddenly expanded channel. **f**, Longitudinal view of a graphene rod showing vertical graphene sheets. **g**, Transverse view of a graphene rod showing horizontal graphene sheets. Inset, transverse section of the graphene rod. **h**, The disappearance of (002) and (004) scattering planes indicates vertical sheets inside the graphene rods with the sheets' planes parallel to the X-ray incident direction. Scale bars, 200 μm (**b**), 0.5 μm (**c**), 200 μm (**f**), 200 μm (**g**), 500 μm (inset of **g**), and 20 nm^{-1} (**d**,**h**).

Flattened sheets are assembled into an anisotropic flat belt structure exhibiting increased orientation order of the sheets (Fig. 1f-h). The orientation order can be further improved by increasing the aspect ratio of the flat microchannel (Fig. 1i), and no pinholes or microvoids occur in the flat graphene belts (Fig. 1j). The centralized dispersion of the characteristic (002) scattering plane indicates a higher order parameter of 0.94, confirming a higher degree of sheet orientation (Fig. 1k and Supplementary Fig. 2). Due to the much improved sheet alignment and orientation order, the graphene belts achieve high tensile strength (1.9 ± 0.1 GPa) and Young's modulus (309 ± 16 GPa) (Fig. 1l). Optimization of the graphene sheet alignment also improves the thermal and electrical conductivities to $1{,}575 \pm 81$ W m^{-1} K^{-1} and $1.04 \pm 0.17 \times 10^6$ S m^{-1}, outperforming commercially available thermally conductive mesophase pitch-based carbon fibres[12,24–26] and previously reported graphene fibres[6,9].

By regulating the elongational and expansion flow patterns during wet spinning, graphene sheet alignment and microstructure can be further tailored with enhanced orientation order (Fig. 2a) at a large scale or with vertically aligned sheets (Fig. 2e), respectively. Specifically, elongational flow through a microchannel with contracted cross-section along the flow direction was created to significantly improve sheet orientation, while coaxial spinnerets with decreased channel cross-sections were designed to generate an elongational flow to fabricate large-sized graphene tubes (Fig. 2b). A high orientation order for the graphene sheets inside tube walls was achieved with contraction flow (Fig. 2c,d) and minimization of the skin effect, leading to an outstanding thermal conductivity of $1{,}260 \pm 47$ W m^{-1} K^{-1} after post annealing. Additionally, well-aligned sheets perpendicular to the flow direction can be created from a step expansion flow (Fig. 2e) by pumping a GO liquid-crystal dispersion from a contracted channel into a suddenly expanded channel. High extensional stress was generated to inversely align the GO sheet orientation from the horizontal to vertical directions, and graphene rods with vertically aligned graphene sheets could be obtained from the step expansion flow (Fig. 2e–g). The equatorial arcs of the (100)/(101) and (102) planes, with disappearance of the (002) and (004) scattering planes on WAXS patterns, further prove the presence of vertically aligned sheets inside the graphene rods (Fig. 2h and Supplementary Fig. 3)[11].

In situ SAXS and computational fluid dynamics simulations

In situ small-angle X-ray scattering (SAXS) was performed to investigate the size and shape confinements and the impact of flow patterns on fluidics-assisted assembly (Figs. 3 and 4). In a static solution, GO sheets are self-assembled into randomly orientated liquid-crystal domains (Supplementary Fig. 4). When a GO solution is pumped through a thin channel, the GO sheets tend to be realigned parallel to the flow direction by the shear stress from the channel wall (Fig. 3a). With increasing flow rates, the isotropic circular SAXS patterns gradually deform into more anisotropic eclipse patterns, suggesting enhancement of the GO sheet alignment during fluidic flow (Fig. 3a). At higher flow velocities, the SAXS patterns and order parameters remain constant (Fig. 3a,b). Saturated GO sheet orientation degree is achieved independent of the flow velocity and is solely determined by the size and shape of the microchannels (Fig. 3a,b). When the GO solution flows in a tubular channel, only 1D orientation order can be observed in the channel axial direction. However, the GO solution flowing in anisotropic flat channels exhibits 2D orientation orders: one from the front face (along the z direction) and the other from the side face (along the y direction) (Fig. 3a). The order parameter of the GO sheets from the side face of a flat channel is higher than that of GO solution flowing in a tubular channel under the same flow velocity (Fig. 3b), and can be further improved for flat channels with lower heights and thus larger aspect ratios (Fig. 3c).

Computational fluid dynamics simulations were performed to understand the flow characteristics and thus fundamental mechanisms of the shape confinements that can manipulate GO sheet alignment during fluid flow. The increase in order parameters with flow rates can be attributed to the enhanced shear stress (Fig. 3d) from the channel wall that deforms and rotates the 2D GO sheets to align parallel to the flow direction. The deformation and rotation of the GO sheets is eventually limited by the confined volume, leading to a saturated sheet orientation order (Fig. 3b). When 2D GO sheets flow in a tubular channel, the GO sheets are aligned in the longitudinal direction, as evidenced by the anisotropic in situ SAXS pattern (Fig. 3a). However, when a mismatch exists in the geometry (for example, 2D planar GO sheets with circular microchannels), the circularly distributed shear stress (Fig. 3e, top) tends to distort and roll up the sheets to match the GO plane with the curved laminar shear stress to reduce flow resistance through the channel. In the lyotropic liquid-crystal solution, the

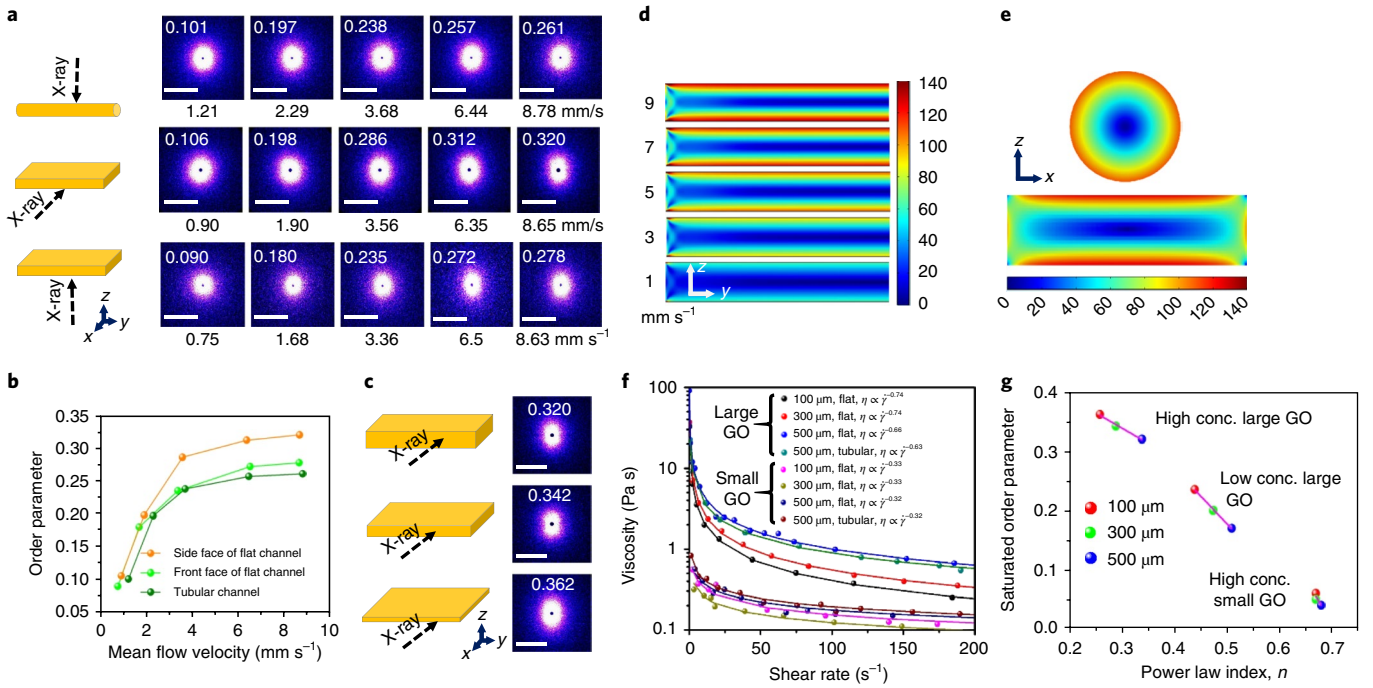

Fig. 3 | Shape and size confinements of microchannels on GO sheet alignment, shear stress/distribution and rheological properties of the fluidic flow. **a**, In situ SAXS patterns of GO fluid at different flow velocities taken from a tubular channel (top, diameter of 500 μm), the side face of a flat channel (middle) and the front face of the flat channel (bottom, height of 500 μm). **b**, Quantitative order parameters of GO sheets calculated based on in situ SAXS patterns from **a** at various flow velocities. **c**, In situ SAXS patterns taken from saturated GO fluids in flat channels with different heights: 500 μm (top), 300 μm (middle) and 100 μm (bottom). **d**, Calculated shear stress on the longitudinal section of the 500 μm flat channel at various inlet flow velocities. The shear stress maps show half channel length (5 mm), representing the entrance region and the developed region. **e**, Calculated shear stress on the transverse section of a 500 μm tubular channel (top) and a 500-μm-thick flat channel (bottom) at the same inlet velocity of 8 mm s^{-1}. **f**, Measured rheological properties of GO solution with large (71 μm) and small (0.5 μm) lateral dimensions in different channels, showing strong shear thinning and size confinement. Solid curves are the fit of experimental data with a power law model. **g**, A linear correlation between saturated order parameters of the GO solution measured by in situ SAXS and corresponding power law index, indicating that the strong size confinement from greater channel size and larger sheet dimensions results in a higher sheet ordering. Solid lines are the fit of experimental data. Scale bar for all SAXS patterns, 1 nm^{-1}. Unit of histogram, Pa (**d**,**e**). The bottom numbers underneath each SAXS pattern in **a** are flow rates. Top inset numbers in **a** and **c** are order parameters calculated from SAXS patterns, characterizing the sheet-to-sheet orientation order at the sub-microscale. *x*, channel side length; *y*, flow direction; *z*, channel height.

GO sheets move in the form of nematic domains, counteracting the rolling force due to the mismatched geometry. Thus, only randomly oriented GO sheets with heavy wrinkles are observed on the cross-section of the columnar fibre spun from tubular channels (Fig. 1b). The wrinkles and distortion of the GO sheets result in misalignment of the sheets with respect to the channel axis, degrading the regularity and orientation order in the longitudinal direction of the fibres.

When a GO solution flows in a flat channel, the flat channel provides a layered and straight distribution of shear stress (Fig. 3e, bottom) for both transverse and longitudinal channel sections, which is more compatible with the geometry of the 2D GO sheets. The flattened GO sheets directed by the channel walls with a compatible geometry are well-aligned in both longitudinal and transverse directions due to the channel shape confinement effect, forming a highly aligned and well-stacked structure (Fig. 1j). The strong shape confinement effect from the flat channel significantly improves orientation orders in the 3D assembly of the resultant belts as compared with curved GO sheets in fibres spun from tubular channels (Fig. 3b).

Channel size confinement occurs when the dimensions of a GO sheet approach those of the microchannel and can be attributed to the enhanced shear thinning degree in lower-height flat channels. Non-Newtonian GO solution shows a shear thinning behaviour during fluidic flow, described by a power law viscosity model, $\eta = K\dot{\gamma}^{n-1}$ (Fig. 3f). With increasing shear rate ($\dot{\gamma}$), the randomly orientated nematic GO phases become more aligned in the direction of the shear stress. Less physical interaction occurs, resulting in a decreased viscosity (η) and power law index, $n < 1$. The shear thinning degree can be quantified by the power law exponent ($n-1$), where the smaller exponent indicates a greater degree of shear thinning. The shear thinning degree of the GO solution has been improved by decreasing the height of the flat microchannels (for example, from 500 to 100 μm) at the same GO concentration of 6 mg ml^{-1} and a sheet lateral size of 71 μm (Fig. 3f). The strong shear thinning enhancement has also been observed in low-concentration GO solutions (2.5 mg ml^{-1}; Supplementary Fig. 5 and Fig. 3g). However, the shear thinning behaviour of the GO solution with smaller sheet size (0.5 μm and 6 mg ml^{-1}) remains constant when flowing in different sized/shaped channels (Fig. 3f), indicating that shear thinning enhancement only happens when the GO lateral size approaches the channel size. When large GO sheets are flowing in lower height channels, the limited space confines the rotational motion of the GO sheets and aligns sheets parallel to the flow direction to reduce viscosity, thus inducing a higher degree of shear thinning (Fig. 3f). The linear correlation between shear thinning degree and saturated sheet orientation order is identified (Fig. 3g). When large dimensional discrepancy exists between the GO sheets and channels, more space is allowed for rotational/flipping motions of the sheets and thus less aligned sheets are observed (Fig. 3c,g), or even randomly distributed small GO sheets in thin channels (0.5 μm GO sheets in a 100-μm-flat channel, Fig. 3g). Using low-height channels, the skin effect can be effectively mitigated as the strong size confinement across the channel transverse section leads to a more uniform sheet ordering.

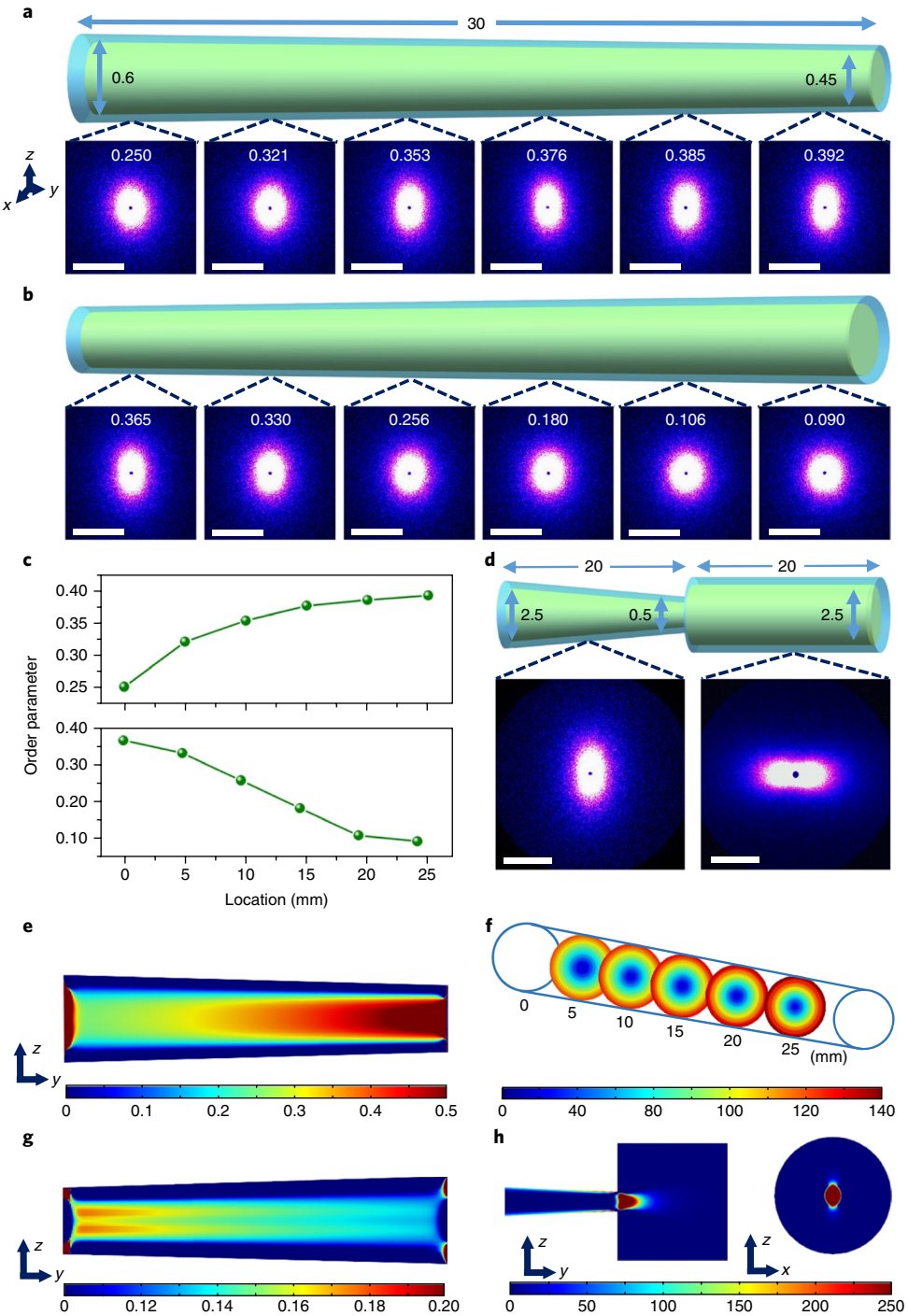

Fig. 4 | Influences of elongational and expansion flow patterns on GO sheet orientation degree and alignment. a,**b**, In situ SAXS patterns taken from GO fluid at different locations during an elongational flow (**a**) and gradual expansion flow (**b**). **c**, Order parameters measured at different locations during elongational and expansion flows. **d**, In situ SAXS patterns taken from GO fluid during a step expansion flow. Rotation of the SAXS patterns indicates that the GO sheet orientation has been changed from the horizontal to the vertical direction. **e**, Calculated elongational rates on the longitudinal section of the channel in **a**. **f**, Calculated shear stress on the transverse sections of the channel in **a**. **g**, Calculated extensional rates on the longitudinal section of the channel in **b**. **h**, Calculated extensional rates on the longitudinal and transverse sections of the channel in **d**. The transverse section is sliced at the inlet of the channel expanded part. The inlet velocity is 10 mm s^{-1} for all calculations. Scale bar for all SAXS patterns, 1 nm^{-1}. Bottom inset numbers in **a** and **b** are order parameters calculated from SAXS patterns. Unit of histograms are s^{-1} in **e**,**g**,**h** and Pa in **f**. Units of dimensions in **a**,**d** are mm.

Manipulating GO sheet orientation and alignment by controlling flow patterns

An elongational flow is generated by using a large tubular channel of gradually shrinking diameter, in which GO solution is pumped to flow from the wide inlet to the narrow outlet (Fig. 4a). The gradually decreasing cross-sectional area of the channel induces a positively increasing elongation rate (dv_y/dy) along the flow direction (Fig. 4e), and accelerates the flow rate and shear stress while decreasing the viscosity (Fig. 4f and Supplementary Fig. 6). Thus, the orientation degree of the GO sheets can be improved in the

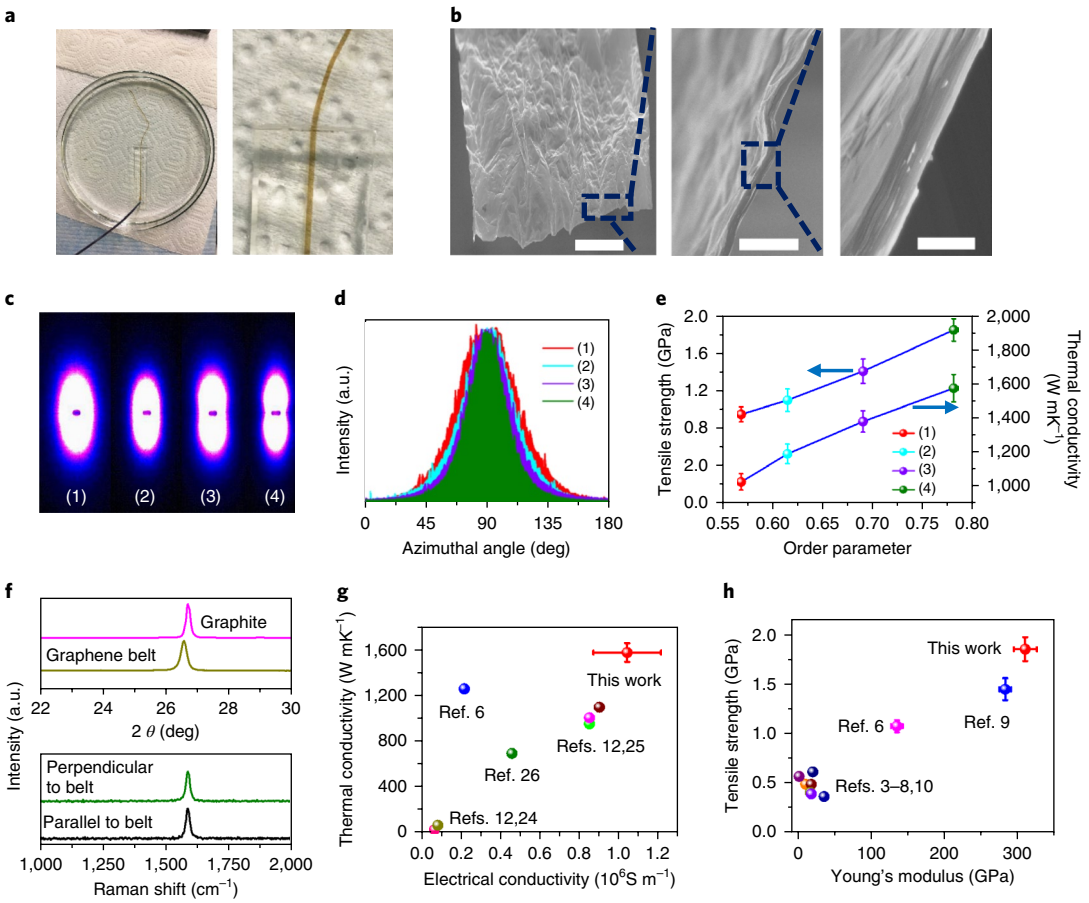

Fig. 5 | Super strong and highly thermally/electrically conductive graphene belts fabricated from flat microchannels. a, Wet spinning of a GO belt by a flat microchannel. **b**, Surface morphology and cross-sectional microstructure of a high-temperature-annealed graphene belt. **c**–**e**, SAXS patterns (**c**), corresponding azimuthal scan (**d**) and structure–property correlation of annealed graphene fibres and belts (**e**). Samples: (1) fibres spun from a tubular channel with a diameter of 160 μm; (2)–(4) belts spun from flat channels with heights of 300, 200 and 100 μm, respectively. Order parameters in **e** are calculated from SAXS patterns in **c**. **f**, XRD and polarized Raman spectra of the annealed graphene belt. **g**, Comparison of electrical and thermal conductivities of graphene belts with the best reported graphene fibres (ref. [10]) and carbon fibres (refs. [19,28–30]). **h**, Comparison of tensile strength and Young's modulus of graphene belts with previously reported graphene fabric structures. Scale bars, 20 μm (**b**, left), 2 μm (**b**, middle) and 0.5 μm (**b**, right). Error bars in **e**,**g**,**h** represent s.d. of five replicas.

direction parallel to the flow direction (Fig. 4a). The less anisotropic SAXS patterns taken from the GO solution at the inlet dramatically deform into a narrow strip at the middle and remain constant when the GO solution passes through the rest of the channel length (Fig. 4a). The calculated order parameters increase rapidly and saturate in the first half-length of the channel (Fig. 4c).

When an expansion flow is generated by reversing the flow direction, the well-aligned GO sheets at the inlet are disrupted and become randomly oriented at the outlet, as evidenced by the deformation of the SAXS patterns and the monotonic decrease in the order parameters along the channel (Fig. 4b,c). The weak perpendicular extensional stress induced in the gradual expansion flow is not sufficient to flip the large GO domains vertically, while the negative elongational rate (Supplementary Fig. 6) results in disruption of the alignment of the GO sheets and a reduction in the order parameters of the GO sheets along the flow direction. Higher inlet velocities (10–30 mm s^{-1}) were applied to increase the extensional rates; however, only randomly oriented GO sheets were observed. Higher extensional rates (dv_z/dz) are required to align the GO sheets perpendicular to the flow direction. In previous studies[27–29], full rotation of the fibre structure was observed to occur in a expansion flow as a result of the low moment of inertia of the fibrils, leading to alignment of the fibre structures perpendicular to the flow direction, despite the low flow rates and weak extensional rate. Here, using a step expansion flow created by pumping GO fluid from a contracted channel into an expanded channel (Fig. 4d), the GO sheets oriented parallel along the flow direction could be fully aligned to the perpendicular direction (Fig. 4d). A sudden inflation of the channel cross-section induced a strong extensional rate (dv_z/dz) at the inlet of the expanded channel section (Fig. 4h), three orders of magnitude higher than that of the gradual expansion flow (Fig. 4g), leading to rearrangement of the GO sheets along the channel perpendicular direction.

High-performance graphene belt

The higher GO sheet order obtained in the fluid flow by means of size/shape confinement or varying flow patterns leads to a better molecular orientation in the final graphene structures (Supplementary Figs. 7 and 8). Anisotropic flat channels enable the fabrication of highly thermally/electrically conductive and mechanically strong graphene belts with a well-aligned and compact structure (Fig. 5a). A monotonically increasing orientation order of the graphene fibres can be identified with GO sheet alignment in fluid flow (Supplementary Figs. 7 and 8). A lower-height channel induces higher orientation degree and

compactness inside graphene belts, without any skin effect across the belt transverse section. The graphene sheets neatly stack into a layer-by-layer graphitic texture without any pinholes or disarrangement (Fig. 5b). In contrast, voids and sheet misalignment can be seen in thick belts spun from larger-height channels, and heavily wrinkled and distorted graphene sheets are observed in columnar fibres spun from tubular channels (Supplementary Fig. 9).

The higher order of graphene alignment is evidenced by the higher anisotropy of the SAXS streak pattern and the narrower distribution of the intensity in the azimuthal direction for the thin graphene belts compared to thick belts and fibres (Fig. 5c,d). Polarized Raman and X-ray diffraction (XRD) spectra were measured to determine the crystallite sizes in 3D (Fig. 5f). The graphene belt has a much larger crystallite size (612 nm) in the transverse direction than the columnar fibre (423 nm), but comparable dimensions for the longitudinal direction and stack height[6,30]. The optimization of sheet alignment, orientation and microstructure (high crystallinity, larger crystallites and the absence of pinhole and structural flaws) leads to superior physical and mechanical properties for the graphene belts (Fig. 5e). The thermal and electrical conductivities of the annealed graphene belt at 2,500 °C reach $1{,}575 \pm 81\ W\ m^{-1}\ K^{-1}$ and $1.0\ (\pm 0.2) \times 10^6\ S\ m^{-1}$, respectively, significantly better than those of mesophase pitch-based carbon fibres or carbon nanotube fibres graphitized at 3,000 °C ($600–1{,}000\ W\ m^{-1}\ K^{-1}$ and $\sim 0.2–0.8 \times 10^6\ S\ m^{-1}$)[24–26,31,32] (Fig. 5g). The fracture strength of the macroscopic graphene belt reaches 1.9 (±0.1) GPa, and the Young's modulus is 309 ± 16 GPa, outperforming the best columnar graphene fibres spun from tubular channels (1.45 and 282 GPa)[9] (Fig. 5h).

Conclusions

Fine control of the sheet alignment and orientation order of macroscopic graphene structures has been realized with microfluidics design, enabling optimization of the microstructure and properties. Strong size and shape confinements are shown to profoundly impact the sheet alignment of the GO sheets during fluidic flow, and also the resultant macroscopic graphene structures. Anisotropic flat channels with high aspect ratios and geometry compatible with the 2D GO sheets allow the fabrication of graphene belts with a higher orientation degree, leading to high thermal, electrical and mechanical properties. Macroscopic graphene structures with high sheet orientation order and tunable alignment direction can be produced by elongational and step expansion flows. The control of different flow patterns offers a unique opportunity for flexibility in tailoring macroscopic graphene structures from perfectly aligned tubes to a 3D open architecture with a vertically aligned graphene sheet arrangement. The mechanisms of the fluidic-assisted assembly in controlling the sheet alignment in the solution as well as the strong size and shape confinements are elucidated. The microfluidics-enabled orientation and microstructure control used to achieve highly ordered graphene structures may be extended to other 2D materials to manufacture hierarchical structures for diverse functional applications.

Online content

Any methods, additional references, Nature Research reporting summaries, source data, statements of data availability and associated accession codes are available at https://doi.org/10.1038/s41565-018-0330-9.

Received: 26 April 2018; Accepted: 20 November 2018;
Published online: 14 January 2019

References

1. Xu, Z. & Gao, C. Graphene chiral liquid crystals and macroscopic assembled fibres. *Nat. Commun.* **2**, 571 (2011).
2. Xu, Z. & Gao, C. Graphene in macroscopic order: liquid crystals and wet-spun fibers. *Acc. Chem. Res.* **47**, 1267–1276 (2014).
3. Dong, Z. et al. Facile fabrication of light, flexible and multifunctional graphene fibers. *Adv. Mater.* **24**, 1856–1861 (2012).
4. Xiang, C. et al. Graphene nanoribbons as an advanced precursor for making carbon fiber. *ACS Nano* **7**, 1628–1637 (2013).
5. Huang, G. et al. Highly strong and elastic graphene fibres prepared from universal graphene oxide precursors. *Sci. Rep.* **4** (2014).
6. Xin, G. et al. Highly thermally conductive and mechanically strong graphene fibers. *Science* **349**, 1083–1087 (2015).
7. Hu, X., Xu, Z., Liu, Z. & Gao, C. Liquid crystal self-templating approach to ultrastrong and tough biomimic composites. *Sci. Rep.* **3** (2013).
8. Zhao, X., Xu, Z., Zheng, B. & Gao, C. Macroscopic assembled, ultrastrong and H_2SO_4-resistant fibres of polymer-grafted graphene oxide. *Sci. Rep.* **3** (2013).
9. Xu, Z. et al. Ultrastiff and strong graphene fibers via full-scale synergetic defect engineering. *Adv. Mater.* **28**, 6449–6456 (2016).
10. Xu, Z., Sun, H., Zhao, X. & Gao, C. Ultrastrong fibers assembled from giant graphene oxide sheets. *Adv. Mater.* **25**, 188–193 (2013).
11. Qin, X., Lu, Y., Xiao, H., Wen, Y. & Yu, T. A comparison of the effect of graphitization on microstructures and properties of polyacrylonitrile and mesophase pitch-based carbon fibers. *Carbon. N. Y.* **50**, 4459–4469 (2012).
12. Emmerich, F. G. Young's modulus, thermal conductivity, electrical resistivity and coefficient of thermal expansion of mesophase pitch-based carbon fibers. *Carbon* **79**, 274–293 (2014).
13. Xin, G. et al. Large-area free standing graphene paper for superior thermal management. *Adv. Mater.* **26**, 4521–4526 (2014).
14. Erik, F., Frank, H. & R, B. M. Carbon fibers: precursors, manufacturing, and properties. *Macromol. Mater. Eng.* **297**, 493–501 (2012).
15. Huang, X. Fabrication and properties of carbon fibers. *Materials* **2**, 2369 (2009).
16. Liu, Y. & Kumar, S. Recent progress in fabrication, structure and properties of carbon fibers. *Polym. Rev.* **52**, 234–258 (2012).
17. Gârlea, I. C. et al. Finite particle size drives defect-mediated domain structures in strongly confined colloidal liquid crystals. *Nat. Commun.* **7**, 12112 (2016).
18. Shen, T.-Z., Hong, S.-H. & Song, J.-K. Electro-optical switching of graphene oxide liquid crystals with an extremely large Kerr coefficient. *Nat. Mater.* **13**, 394–399 (2014).
19. Maiti, U. N., Lim, J., Lee, K. E., Lee, W. J. & Kim, S. O. Three-dimensional shape engineered, interfacial gelation of reduced graphene oxide for high rate, large capacity supercapacitors. *Adv. Mater.* **26**, 615–619 (2014).
20. Wang, G. et al. Flexible pillared graphene-paper electrodes for high-performance electrochemical supercapacitors. *Small.* **8**, 452–459 (2012).
21. Seo, D. H., Han, Z. J., Kumar, S. & Ostrikov, K. Structure-controlled, vertical graphene-based, binder-free electrodes from plasma-reformed butter enhance supercapacitor performance. *Adv. Energy Mater.* **3**, 1316–1323 (2013).
22. Li, G., Zhang, X., Wang, J. & Fang, J. From anisotropic graphene aerogels to electron- and photo-driven phase change composites. *J. Mater. Chem. A* **4**, 17042–17049 (2016).
23. Håkansson, K. M. O. et al. Hydrodynamic alignment and assembly of nanofibrils resulting in strong cellulose filaments. *Nat. Commun.* **5**, 4018 (2014).
24. Qiu, L., Zheng, X. H., Zhu, J., Su, G. P. & Tang, D. W. The effect of grain size on the lattice thermal conductivity of an individual polyacrylonitrile-based carbon fiber. *Carbon* **51**, 265–273 (2013).
25. Yuan, G. et al. The structure and properties of ribbon-shaped carbon fibers with high orientation. *Carbon* **68**, 426–439 (2014).
26. Gallego, N. C. et al. The thermal conductivity of ribbon-shaped carbon fibers. *Carbon* **38**, 1003–1010 (2000).
27. Trebbin, M. et al. Anisotropic particles align perpendicular to the flow direction in narrow microchannels. *Proc. Natl Acad. Sci. USA* **110**, 6706–6711 (2013).
28. Vincent, M. & Agassant, J. F. Experimental and theoretical study of short fiber orientation in diverging flows. *Rheol. Acta* **24**, 603–610 (1985).
29. Kiriya, D., Kawano, R., Onoe, H. & Takeuchi, S. Microfluidic control of the internal morphology in nanofiber-based macroscopic cables. *Angew. Chem. Int. Ed.* **51**, 7942–7947 (2012).
30. Cançado, L. G. et al. General equation for the determination of the crystallite size La of nanographite by Raman spectroscopy. *Appl. Phys. Lett.* **88**, 163106 (2006).
31. Gspann, T. S. et al. High thermal conductivities of carbon nanotube films and micro-fibres and their dependence on morphology. *Carbon* **114**, 160–168 (2017).
32. Adams, P. M., Katzman, H. A., Rellick, G. S. & Stupian, G. W. Characterization of high thermal conductivity carbon fibers and a self-reinforced graphite panel. *Carbon* **36**, 233–245 (1998).

Acknowledgements

This work was supported financially by the US National Science Foundation under the award no. DMR 1742806. Thermal conductivity measurement of the macroscopic graphene structures was supported by the US National Science Foundation under the award CMMI 1463083.

Author contributions

G.X. and J.L. designed the research. G.X. and Y.D. designed the microfluidic channels. G.X and W.Z. collected and analysed thermal, mechanical and microstructure data. G.X., Y.D., J.C. and L.T.Z. performed computational fluid dynamics simulations. G.X., A.J.C., S.D. and J.L. co-wrote the paper. All authors discussed the results and commented on the manuscript.

Competing interests

The authors declare no competing interests.

Additional information

Supplementary information is available for this paper at https://doi.org/10.1038/s41565-018-0330-9.

Correspondence and requests for materials should be addressed to J.L.

Methods

Materials. Graphite intercalation compounds (99.99%, 50 mesh) were purchased from Qingdao Nanshu Graphite Co. $K_2S_2O_8$ (99%), P_2O_5 (98%) and sodium nitrate (99%) were purchased from Sigma Aldrich. HCl (36.5%), ethanol (95%) and H_2SO_4 (98%) were purchased from Fisher Chemical. $KMnO_4$ (99.4%) was purchased from Mallinckrodt Specialty Chemicals. H_2O_2 (30%) was purchased from Macron Fine Chemicals. Polydimethylsiloxane (PDMS, Sylgard 184) was purchased from Dow Corning.

Synthesis of GO solutions. GO was prepared from graphite powders following a modified Hummers' method[6,9]. Briefly, the graphite intercalation compounds were expanded at 750 W by microwave irradiation for 90 s to obtain worm-like expanded graphite. The expanded graphite powders (5 g), concentrated H_2SO_4 (300 ml), $K_2S_2O_8$ (4.2 g) and P_2O_5 (6.2 g) were added successively into a flask (500 ml) and the mixture was kept at 80 °C for 24 h. After cooling to room temperature, the mixture was diluted with de-ionized water then vacuum-filtered and washed with de-ionized water until pH neutral. The expanded graphite powder was dried in air at room temperature for 2 days. After drying, the expanded graphite (5 g) was added to a mixture containing concentrated H_2SO_4 (115 ml) and $NaNO_3$ (2.5 g) in an ice bath (0 °C). $KMnO_4$ (15 g) was then added carefully to the solution and maintained for 30 min at 35 °C followed by a slow addition of de-ionized water (230 ml). The temperature of the reaction was maintained at 98 °C for 15 min. Additional de-ionized water (355 ml) containing H_2O_2 (3 wt%, 50 ml) was added. The solid obtained from centrifugation (8,000 r.p.m., 5 min) was washed with excess de-ionized water, 20 vol% HCl and ethanol. The washing process was repeated several times until the pH of the solution reached neutral. A final aqueous solution of large GO sheets was thus obtained. To obtain small GO sheets, the large GO solution was sonicated by a tip (bar type) sonication instrument at 500 W for 1.5 h (Supplementary Fig. 11).

To obtain a GO/DMF solution for wet spinning, the water solvent in the GO dispersion was replaced by DMF by centrifuging the dispersion in water at 8,000 r.p.m. for 15 min to remove the supernatant. The obtained GO solid was dispersed in DMF and centrifuged to remove the supernatant. The DMF washing process was repeated five times to achieve the final concentrated GO/DMF solution.

In situ SAXS microchannel fabrication. Flat microchannels with a thin glass window were fabricated to withstand high pressure and to obtain a high X-ray transmission for in situ X-ray measurements. Stainless steel sheets of different thicknesses (100–500 μm) and 3 mm width were used as a mould. Two flat microchannels with different configurations were fabricated for the SAXS measurement on the front face and side face.

For the SAXS measurement on the side face, the flat microchannel was fabricated with stainless steel sheets standing in a 4 inch plastic Petri dish. PDMS pre-polymer (Sylgard 184; Dow Corning) was poured into the Petri dish until the liquid surface and upper edge of the steel mould were at the same level. The PDMS was then degassed and cured at 80 °C overnight. The PDMS replica was removed from the stainless steel mould, and inlet ports were punched into the polymer from the side face. The thin layer of PDMS covering the channel on the top surface was removed. A microscope cover glass (thickness, 170 μm) was etched with buffered oxide etchants to decrease the thickness to 20 μm. The top and bottom surfaces of the PDMS replica and thin glass surface were treated with a plasma cleaner. The PDMS replica was then sealed with the glass to form channels. Channels were incubated overnight in a convection oven at 65 °C. For the front face SAXS measurement, the PDMS microchannel was fabricated with a similar procedure, but the stainless steel mould was laid down in the plastic Petri dish instead of standing.

For the SAXS measurements for a tubular channel, a thin-walled (10 μm) capillary (Charles Supper Company) with an outer diameter of 400–700 μm was applied. PTFE tubes were connected to the capillary to pump the GO solution through the capillary during the SAXS measurements. For SAXS measurements on the contracted, gradually expanded channel and step expanded channel, thin-walle d(10 μm) capillaries with dimensions as shown in Fig. 4 were applied.

Fabrication of microchannels for wet spinning of graphene belts. Microchannels were fabricated by standard single-layer photolithography[33]. Briefly, SU-8 3050 photoresist (Microchem Co.) was spin-coated on silicon wafers and sequentially baked at 65 and 95 °C. A photomask containing microfluidic channel patterns was used for ultraviolet exposure. The patterning process was completed after a post-exposure bake (95 °C) and a development process, thus generating the mould. After pouring PDMS resin into the mould and curing at 65 °C for 2 h, the cured PDMS was retrieved. PDMS replicas were treated along with the glass substrates by a plasma cleaner and bonded together to form channels. The final dimensions of the PDMS microchannel were 100–300 μm (height) by (500–3,000 μm width) by 5 cm (length).

Fabrication of graphene belts, tubes and rods. Following the wet-spinning protocol outlined in the literature[6,9], GO/DMF spinning solution was injected into coagulation baths from the microchannels and a coaxial spinneret to obtain belts and tubes, respectively. After a 30 min immersion in coagulation baths, the GO gel belts and tubes were suspended over two parallel rods in the air to dry overnight. During drying, the distance between parallel rods was extended by around 10% to apply a tensile stress on the belts and tubes to enhance sheet alignment. GO rods were obtained by directly injecting GO aqueous dispersion from the step expansion channel into liquid nitrogen baths. The frozen GO rods were collected and freeze-dried.

As-spun GO structures were first reduced with HI vapour at 80 °C overnight. During reduction, belts and tubes remained fixed on the parallel rods under tensile stress. The reduced GO structures were then fixed on a graphite fixture and annealed using a tube furnace. The samples were heated from room temperature to 1,000 °C at a rate of 1 °C min^{-1} and maintained at this temperature for 1 h in a flow of argon. High-temperature annealing was conducted with an electrical furnance. The samples were heated from room temperature to 2,500 °C at a rate of 1,000 °C h^{-1} and maintained at this temperature for 1 h in a flow of argon.

Characterizations. The morphology and microstructure of the graphene structures were characterized by a field-emission scanning electron microscope (JEOL JSM-6335). X-ray photoelectron spectroscopy was carried out on a PHI 5000 Versa Probe system (Supplementary Fig. 12). Raman studies of graphene structures were performed with a LabRAM HR800 Raman microscope using a 532.18 nm green laser beam as the probing light source and a 600 gr mm^{-1} grating. The crystallite dimensions (L_a) were determined using the empirical formula[30,34] L_a (in nm) $= (2.4\times10^{-10})\lambda^4(I_D/I_G)^{-1}$, where λ is the laser wavelength and (I_D/I_G) is the integrated intensity ratio of the D and G bands. XRD was performed using a PAN analytical X-ray diffraction system with a source wavelength of 1.542 Å at room temperature. The phase change enthalpy of graphene tube encapsulated phase change materials was measured with a differential scanning calorimeter (TA Instruments Q100). Tensile strength testing was conducted using an Instron 5843 electro-mechanical test system with 20 mm gauge length and 0.5 mm min^{-1} extension rate. The thermal conductivity of thermal interfacial materials embedded with vertically aligned graphene sheets was measured with a Netzsch LFA 457 NanoFlash instrument. A FLIR A325sc infrared camera was used to record heat transport on various samples.

Thermal conductivity measurements for the 1D graphene fibre, belt and tube. The effective thermal conductivities of the graphene fibres, belts and tubes were measured using a well-established self-heating method[6,35]. The measurements were carried out using the apparatus described in ref. [6]. Briefly, the measurement was performed in a vacuum chamber with a zinc selenide viewport. Two copper blocks were applied as heat sinks. A 1D graphene sample (fibre, belt and tube) was suspended between heat sinks and high-purity silver paste was applied at the ends to obtain high-quality contacts and maintain the temperature of the sample ends at ambient temperature, T_a. A direct current was applied to the sample, thus changing the temperature of the samples. A FLIR A325sc infrared camera with a close-up lens was used to measure the temperature profile along the samples through the zinc selenide viewport.

During measurements, the 1D heat transfer problem was considered because the diameter of the sample was much smaller than the length. When the temperature rise is not large (below 40 °C in this study), we can assume that the volumetric heat generation due to Joule heating, $\dot{q} = UI/2LA_c$, is uniform, where A_c is the cross-section area of the sample, and U and I are the voltage and current measured across the contacts, respectively. When the origin of x is set at the middle point of the suspended sample, the 1D steady-state heat transfer equation can be written as

$$-kA_c\frac{d^2T}{dx^2} + hp(T-T_a) = \frac{UI}{2l} \quad (1)$$

where p is the perimeter of the cross-section and k and h are the thermal conductivity and heat transfer coefficient, respectively. The tests were carried out under high vacuum (10^{-4} torr) to eliminate convective heat transfer. When the temperature increase is small, the heat loss to the surroundings accounted from convection and radiation can be neglected. We can then rewrite the equation as

$$k\frac{d^2T}{dx^2} + \dot{q} = 0 \quad (2)$$

With boundary conditions at the two ends of the sample given by $T_L = T_a$ and $T_{-L} = T_a$, the temperature distribution of the sample can be expressed as

$$T_x = T_a + \frac{\dot{q}}{2k}(L^2 - x^2) \quad (3)$$

The temperature was distributed symmetrically with respect to the middle point ($x = 0$) of the sample, where the highest temperature (T_0) was achieved. An infrared thermal image of a self-heated sample at steady state (Supplementary Fig. 13a) shows that the highest temperature occurs at the middle and the temperature decreases gradually as it approaches the heat sink. The temperature profile along the sample clearly resembles a parabolic curve (Supplementary Fig. 13b), matching the trend from theoretical calculations very well. After measuring T_0 at the middle

point and T_a at the end of the sample with a high-performance infrared camera, the thermal conductivity of the sample can be obtained from

$$k = \frac{UIL}{4A_c(T_0 - T_a)} \quad (4)$$

To minimize experimental uncertainty, a series of T_0 measurements were taken at various increased heating powers (UI) by increasing the current. The thermal conductivity (k) was obtained from the slope of the linear fitting $T_0 - T_a$ and UI. Supplementary Fig. 1c shows the relationship between the rise of the middle point temperature and the heating power from a typical self-heated belt. As expected, the $T_0 - T_a$ increases linearly with heating power, ensuring the accuracy of the thermal conductivity measurement. Therefore, the effect of convective and radiative heat transfer can be neglected without causing significant error in our experiments, as convective and radiative heat transfer would result in a nonlinear relationship. The measurement system was further calibrated by measuring the thermal conductivity of graphite microribbons sliced from graphite films with known thermal conductivities of ~624 W m^{-1} K^{-1} and 1,100 W m^{-1} K^{-1}, measured with a laser flash method using a Netzsch LFA 457 NanoFlash instrument. The measured values from our apparatus were ~650 W m^{-1} K^{-1} and 1,030 W m^{-1} K^{-1}, identifying a difference of less than 7% within the range of experimental uncertainty.

In situ SAXS and WAXS test. WAXS and SAXS measurements were carried out on a Bruker Nanostar-U instrument with a rotating anode X-ray source, operated at 50 kV and 24 mA. The SAXS detector was a multi-wire proportional counter (Bruker Hi-Star) with 1,024 × 1,024 pixels and a beryllium front window 11.5 cm across. The SAXS detector was placed 105 cm from the sample, allowing measurement of scattering angles from 0.2 to 2.8° (2θ). The WAXS detector was an image plate (a Fuji FLA-7000 system, ~20 × 25 cm in size). During in situ SAXS data collection, a microchannel was placed horizontally and GO solution was pumping through the microchannel at different flow rates. During WAXS measurement, the graphene fibres, belts, tubes and rods were fixed in the vertical direction.

Calculation of order parameters. Quantification of the SAXS and WAXS patterns was performed with scattering vector q (defined as $q = 4\pi \sin\theta/\lambda$, where 2θ is the scattering angle) and azimuthal angle φ as coordinates. The GO sheet orientation distribution during flow was then found by summing in the range $0.2 < q < 2$ nm^{-1} for SAXS measurements. SAXS could thus be used to characterize the sheet-to-sheet orientation order on a submicrometre scale. In contrast, WAXS measurements were carried out for a scattering angle range of 0.2–70° and could be applied to characterize the orientation order at the atomic scale. The orientation of the graphene sheets in fibres and belts was quantified by the (002) reflection on the WAXS patterns.

The GO sheet orientation and graphene sheet alignment were quantified by converting the orientation distribution into a Hermans order parameter, h, defined as[23]

$$h = \left\langle \frac{3}{2}\cos^2\varphi - \frac{1}{2} \right\rangle \quad (5)$$

where φ is the azimuthal distribution, and the order parameter can be expanded as

$$h = \int_0^{\pi} I(\varphi)\left(\frac{3}{2}\cos^2\varphi - \frac{1}{2}\right)\sin(\varphi)\,\mathrm{d}(\varphi) \quad (6)$$

The intensity is normalized according to

$$\int_0^{\pi} I(\varphi)\sin(\varphi)\,\mathrm{d}(\varphi) = 1 \quad (7)$$

GO rheological property measurement. Various GO solutions with different GO sizes (large, 71 μm; small, 0.5 μm) and concentrations (high, 6 mg ml^{-1}; low, 2.5 mg ml^{-1}) were pumped through different microchannels by a pressure controller (Elveflow OB1 Mk3). The pressure drop was read directly from the pressure controller. The flow rate was obtained by dividing the volume of pumped GO solution over the time interval. The shear rate and viscosity were calculated based on ref. [36].

Computational fluid dynamics simulations. The non-Newtonian flow behaviour of the GO solution was characterized by a shear rate-dependent viscosity. The shear rate–viscosity data from rheology measurements were fitted by the power law viscosity model $\eta = K\dot{\gamma}^{n-1}$ (plotted in Fig. 3f) and applied into simulations.

The dynamics of the velocity field $\mathbf{v}$ of the incompressible non-Newtonian fluid are described by the Navier–Stokes equation with the shear rate-dependent viscosity:

$$\nabla \cdot \mathbf{v} = 0 \quad (8)$$

$$\rho\partial_t \mathbf{v} + \rho(\mathbf{v}\cdot\nabla)\mathbf{v} = \nabla \cdot [-pI + \eta(\nabla\mathbf{v} + \nabla\mathbf{v}^T)] \quad (9)$$

with constant density of the fluid ρ and unity matrix I.

The equation was solved with COMSOL Multiphysics v5.2a software. In a first step, the designed microchannel geometry is built in COMSOL and finite elements are generated based on the geometry. Boundary conditions are assigned to the elements to match the experiment conditions. Shear stress, elongational rate, extensional rate and viscosity distribution are obtained from the simulation.

Data availability

The data that support the plots within this paper and other findings of this study are available from the corresponding author upon reasonable request.

References

33. Wu, Z., Chen, Y., Wang, M. & Chung, A. J. Continuous inertial microparticle and blood cell separation in straight channels with local microstructures. *Lab Chip* **16**, 532–542 (2016).
34. Endo, M. et al. Structural analysis of the B-doped mesophase pitch-based graphite fibers by Raman spectroscopy. *Phys. Rev. B* **58**, 8991–8996 (1998).
35. Zhang, L., Zhang, G., Liu, C. & Fan, S. High-density carbon nanotube buckypapers with superior transport and mechanical properties. *Nano Lett.* **12**, 4848–4852 (2012).
36. Son, Y. Determination of shear viscosity and shear rate from pressure drop and flow rate relationship in a rectangular channel. *Polymer* **48**, 632–637 (2007).